ACS OMEGA

http://pubs.acs.org/journal/acsodf

Article

Property and Reactivity Relationships of Co_3O_4 with Diverse Nanostructures for Soot Oxidation

Chao Hu,* PengCheng Dai, Zhenzhen Chen, and Haitao Zhang*

Cite This: *ACS Omega* 2022, 7, 44116−44123

Read Online

ACCESS | Metrics & More | Article Recommendations

ABSTRACT: Cobalt oxide (Co_3O_4) nanostructures with different morphologies (nanocubes, nanoplates, and nanoflowers) were synthesized by a simple hydrothermal method and used for catalytic oxidation of soot particles. Through the study of the physicochemical properties of the catalysts, the key factors affecting the performance of soot oxidation were investigated. The results showed that all three kinds of Co_3O_4 nanocrystals exhibited excellent low-temperature activity in catalytic oxidation of soot, and the Co_3O_4 nanoflowers showed higher oxidation activity of soot compared with Co_3O_4 nanocubes and Co_3O_4 nanoplates, whose T_m was only 370 °C. The excellent activity of Co_3O_4 nanoflowers was due to the large amount of Co^{3+} and lattice oxygen on their surface and highly defective structure, which promoted the adsorption and activation of oxygen species. The large crystallite size and few surface defects were the main reasons for the poor catalytic performance of Co_3O_4 nanocubes. During soot oxidation, the crystallite size of the catalysts and the contact between the catalysts and soot played a significant role in the catalytic performance.

1. INTRODUCTION

Diesel exhaust contains many pollutants, such as particulate matter, nitrogen oxides (NO_x), and unburned hydrocarbons, which are harmful to human health and severely pollute the environment.[1] Owing to their small size, soot particles can be inhaled by the human body, causing asthma, bronchitis, lung cancer, and other diseases.[2] Soot particles are produced on burning hydrocarbon fuels. They are mainly carbon particles, containing a mixture of graphite sp^2-bonded carbon and other mixed particles of organic and inorganic matter.[3,4] Soot particles appear as necklace-like agglomerates.[5]

Recently, diesel particulate filters (DPFs) have become the most economical, safe, and reliable exhaust aftertreatment technology for removing soot particles. However, soot particles accumulate on the filter, affording decreased filtration efficiency and increased engine backpressure. The spontaneous combustion temperature of soot particles is above 600 °C, and the engine exhaust temperature is between 200 and 500 °C.[6] It is an effective way to achieve active regeneration of DPFs by strategically injecting fuel to burn soot. However, this approach causes a high-temperature increase, which may damage DPFs and not be conducive to the fuel economy.[7] Currently, catalytic combustion and DPFs are the most commonly used post-treatment technology. In this technology, the DPF traps soot particles in tail gas, reduces the spontaneous combustion temperature of soot using a catalyst, and makes soot burn at the diesel engine's exhaust temperature to realize the periodic passive regeneration of the filter.[8,9]

A suitable catalytic system is the key to lowering the soot oxidation temperature. Recently, a range of highly efficient catalysts such as noble metals, alkali metals, transition metal oxides, perovskite oxides, and rare earth oxides have shown good performances for removing soot particles.[10] To reduce the cost, several studies have focused on developing non-noble metal catalysts. Transition metal oxides exhibit an excellent redox performance owing to the change in valence in the oxidation reaction. Thus, they are widely used in catalytic chemistry in the fields of electrochemistry, formaldehyde catalytic oxidation, CO oxidation, and soot oxidation.[11−14]

Among them, cobalt oxides are inexpensive and have gained increasing attention, owing to their excellent catalytic activity in volatile organic compound (VOC) sensors, electrochemistry, high alcohol synthesis, phenol oxidation, methane, toluene combustion, soot catalytic oxidation, and many other fields.[15] Co_3O_4 nanorods exhibited good stability, high sensitivity, and fast response and recovery time to detect VOCs.[16] Co_3O_4 cube nanoelectrodes exhibited better sensitivity and lower limit of detection through the comparative study of the Co_3O_4 spheres and cubes for H_2O_2 electrochemical detection.[17] Furthermore, Co_3O_4 nanooctahedrons had a strong long cycle and rate performance, good structural durability, and low charge transfer resistance,

Received: August 28, 2022
Accepted: November 15, 2022
Published: November 23, 2022

showing excellent electrochemical performance, through the study of the lithium storage properties.[18,19] The Co_3O_4 hollow octahedral cage showed low initial irreversible loss and very high reversible capacity.[20] Ouyang et al. found that Co_3O_4 (nanorods and nanowires)-supported Pt catalysts had stable CO_2 conversion and alcohol selectivity within 50 h, and some oxygen vacancies on the active surface of the Pt−Co_3O_4-p catalyst made it easier to be reduced.[21] Moreover, Co_3O_4 nanorods exhibited excellent catalytic activity in the oxidation of phenol by the sulfate group, and they had good stability and small inactivation in several studies.[22] Furthermore, Co_3O_4 exhibits excellent activity in catalytic combustion. Hu et al. found that in the catalytic combustion of methane, the catalytic activity follows the order Co_3O_4 nanowires > Co_3O_4 nanoribbons > Co_3O_4 nanocubes.[23] Ren et al. found that 3D-Co_3O_4 nanoflowers had a large specific surface area and rich surface active oxygen, which improved their oxidation ability. Furthermore, the catalytic activity of 3D-Co_3O_4 nanoflowers did not considerably decrease within 120 h, suggesting that the nanoflowers had long-term stability for toluene combustion.[24] In terms of CO oxidation, Wang et al. found that Co_3O_4 nanorods showed excellent CO catalytic activity and durability owing to many oxygen defects on their surface.[25] Hu et al. reported that Co_3O_4 nanoribbons had higher catalytic activity than Co_3O_4 nanocubes in CO oxidation because the Co^{3+} sites on the (011) plane were more active than those on the (001) plane.[26] The importance of the shape and crystal plane effect has been proved, which is important for developing shape-controllable nanocrystal model catalysts. Given the soot catalytic combustion of Co_3O_4, Zhai et al. showed that Co_3O_4 nanocubes with exposed (001) surfaces had more active Co^{3+} and enhanced redox properties and surface lattice oxygen mobility, showing improved soot catalytic efficiency.[27] Meanwhile, Co_3O_4 nanocubes had a clear shape, stable crystal phase, and strong stability to structural collapse.

The catalytic oxidation of soot is a typical heterogeneous catalytic reaction, which occurs at the three-phase boundary between the solid catalyst, soot particles, and the gas reaction (solid−solid−gas).[28] There are two main factors affecting the catalytic activity of soot: the contact efficiency between the soot and catalyst and the intrinsic activity of the catalyst.[27] To improve the catalytic oxidation activity of soot, the catalyst must be modified in the following two ways. First, the surface characteristics of catalysts play a key role in determining the combustion efficiency of soot.[29] Second, the role of catalysts is to transfer active oxygen species to the surface of soot to enable soot oxidation.[30] Therefore, it is necessary to design catalysts with an acceptable structure to expand the contact efficiency between soot and catalysts. Finding catalytic materials with high intrinsic activity is the main research task. Although many efforts have been made in the aspect of the facet-dependent reactivity of Co_3O_4 nanocrystals, the essential correlation between the physicochemical properties of Co_3O_4 and its performance in catalyzing soot oxidation is unclear. Herein, Co_3O_4 with various nanostructures (nanotubes, nanoplates, and nanoflowers) is expected to produce a new and more efficient catalyst for soot particle oxidation. Three types of Co_3O_4 nanocrystals with different facets were synthesized using a simple hydrothermal method. The structural morphology and physicochemical properties of the catalyst were studied using X-ray diffraction (XRD), Raman spectroscopy, Fourier transform infrared spectroscopy (FTIR), and scanning electron microscopy (SEM).[31,32] The redox properties of the samples were studied via hydrogen−temperature-programmed reduction (H_2−TPR) and oxygen−temperature-programmed desorption (O_2−TPD),[33] The structure and electronic properties of the catalyst were studied using X-ray photoelectron spectroscopy (XPS).[34] Through the study of Co_3O_4 nanocrystals with different facets, the oxidation efficiency of catalysts with different facet shapes of the same element is explored. This is expected to prepare more efficient catalysts in the field of soot catalysis.

2. EXPERIMENTAL SECTION

2.1. Catalyst Preparation. Co_3O_4 nanocrystals with diverse nanostructures, including nanocubes, nanoplates, and nanoflowers, were synthesized using a template-free hydrothermal synthesis method. Certain amounts of $Co(NO_3)_2 \cdot 6H_2O$ and 0.02 mol NaOH were dissolved in 80 mL of deionized water via magnetic stirring for 30 min. The resulting solution was transferred to a stainless-steel autoclave lined with polytetrafluoroethylene (PTFE) and reacted at 180 °C for 5 h. The reaction was centrifuged five times with deionized water after cooling to room temperature (25 °C), dried at 80 °C for 24 h, and finally calcined at 500 °C for 4 h in air. The resulting Co_3O_4 nanocubes were labeled Co-c.

Co_3O_4 nanoplates were synthesized using the following procedure. A certain amount of $Co(NO_3)_2 \cdot 6H_2O$ was dissolved in a mixture containing 10 mL of ethanol and 10 mL of deionized water and stirred to form a clear solution. Subsequently, 0.8 g of NaOH was dissolved in 50 mL of deionized water and added to the abovementioned solution. The resulting solution was stirred for 30 min, transferred to a stainless-steel autoclave lined with PTFE, sealed, and heated to 100 °C for 12 h. The synthesized product was centrifuged five times with deionized water after cooling to room temperature, dried at 80 °C overnight, and finally calcined at 300 °C for 3 h in air. The Co_3O_4 nanoplates obtained were called Co-p.

Co_3O_4 nanoflowers were synthesized using the following procedure. A certain amount of $Co(NO_3)_2 \cdot 6H_2O$ was dissolved in 20 mL of deionized water, mixed with 4 g of urea, and stirred for 30 min. The resulting mixture was transferred to a stainless-steel autoclave lined with PTFE and kept in an oven at 110 °C for 12 h. After cooling to 25 °C, the synthesized product was centrifuged five times with deionized water and dried overnight in an oven at 50 °C. Finally, it was calcined at 300 °C for 3 h in air. The resulting Co_3O_4 nanoflowers were labeled Co-f.

2.2. Catalyst Characterizations. The crystallographic information of Co_3O_4 with various nanostructures was obtained by the XRD method and compared with the diffraction peak of the standard card to determine the crystalline phases of the samples. XRD analysis of the catalysts was carried out using an Ultima IV X-ray diffractometer from Japan. Copper target Ka radiation, power 3 KW, scan speed 10° min^{-1}, and scan angle 10−80°.

The specific surface areas and pore size distributions of the catalyst samples were measured by nitrogen adsorption at liquid nitrogen temperature using a surface area analyzer (ASAP 2460, Micromeritics).

The micromorphology and grain size of the catalyst samples were measured using a Zeiss Sigma 300 scanning electron microscope. The field emission was 15 kV acceleration voltage. Before the test, gold was sprayed on the sample for 30 s to enhance the conductivity of the samples.

https://doi.org/10.1021/acsomega.2c05550
ACS Omega 2022, 7, 44116−44123

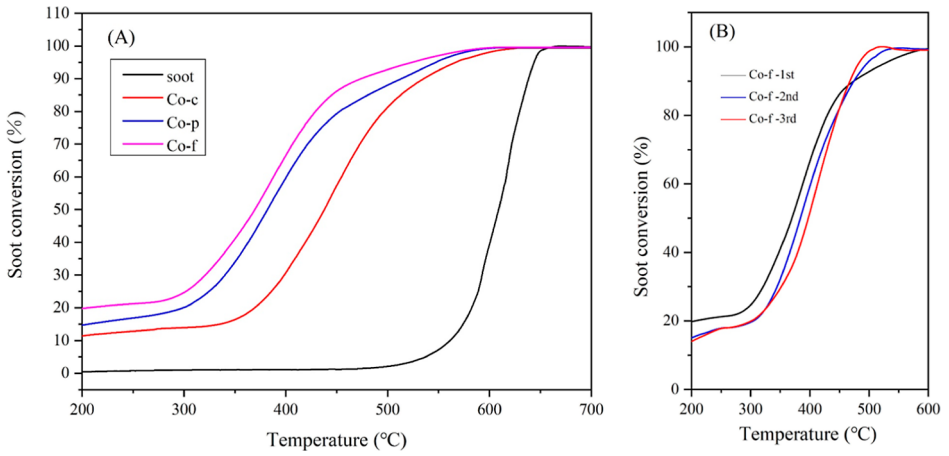

Figure 1. (A) Catalytic performance of Co_3O_4 on soot oxidation and (B) stability tests of catalyst Co-f.

H_2−TPR and O_2−TPD were performed using a PCA-1200 chemisorption analyzer. The 30 mg samples were pretreated in a nitrogen atmosphere at 100 °C for 10 min. After dropping to room temperature, the samples were purged with a mixture of nitrogen and hydrogen/argon oxygen, and the TCD was turned on. After the baseline was stabilized, the temperature was increased to 900 °C with 10 °C min^{-1} program.

Raman spectroscopy is an important way to detect the surface defects of catalysts. The Raman spectrum analysis was carried out on the Thermo Fisher DXR2 explicit differential spectrometer with an excitation wavelength of 532 nm and a laser power of 3 MW.

FTIR adopted the Fourier transform infrared spectrometer Tensor 27 of Bruker company in Germany, with a resolution of 4 cm^{-1} and a scanning range of 400−4000 cm^{-1}. First, potassium bromide was ground into fine particles; then, the catalyst sample and potassium bromide were mixed and ground for 5 min according to a mass ratio of 1 to 100 MPa, the mixture was fully refined to prevent the effect of scattering on the spectrum, the tablets were pressed under a pressure of 10 MPa in the tablet press, and the samples with good permeability were put into the instrument for testing.

The element composition and main valence state of the catalyst were tested by XPS. The photoelectric spectrometer Thermo Scientific K-Alpha was used in the experiment, the Al Ka ray ($h\nu$ = 1486.6 eV) was used as the X-ray source, the voltage was 12 kV, and the C 1s = 284.80 eV binding energy (BE) was used as the energy standard for charge correction.

2.3. Catalyst Activity Evaluation. This experiment used Printex-U carbon black (Degussa, Germany) with a particle size of 25 nm to substitute the soot particles in exhaust. The catalyst activity was evaluated via thermogravimetric analysis (TGA, TGA-Q500). Briefly, 5 mg of soot particles and 50 mg of the catalyst were mixed well in a mass ratio of 1:10. The mixed samples were placed on an aluminum crucible and heated from room temperature to 800 °C at a heating rate of 10 °C min^{-1} in air (100 mL/min). The catalytic activity of the catalysts for soot oxidation was evaluated by measuring the mass change in soot particles before and after the reaction and by calculating the conversion rate of soot particles. 1-1 presents the formula for calculating the soot conversion rate.

$$\eta = \frac{[\text{Soot}]_A - [\text{Soot}]_B}{[\text{Soot}]_A} \times 100\% \quad (1\text{-}1)$$

where η is the soot conversion rate, $[\text{Soot}]_A$ is the soot quality before the reaction, and $[\text{Soot}]_B$ is the soot quality after the reaction. The catalyst activity associated with the catalytic oxidation process of soot particles was evaluated based on the soot-particle conversion temperatures. T_{50} and T_{90} represented the temperatures when the soot particle conversion rates were 50 and 90%, respectively, and T_m is the maximum oxidation rate temperature. When the conversion rate is the same, a smaller value means the catalyst has a better catalytic effect on soot particles.

3. RESULTS AND DISCUSSION

3.1. Catalytic Performances of Co_3O_4 for Soot Oxidation. Figure 1 shows the conversion curve of the oxidation process of soot particles catalyzed by Co_3O_4 and the stability tests of catalyst Co-f. Table 1 summarizes the T_{50}, T_{90}, and T_m of the catalyst samples and compares the activity of some Co_3O_4 catalysts reported for soot oxidation. Soot begins to oxidize at 500 °C without a catalyst, and T_m is 620 °C, as shown in Figure 1. Using the catalyst, the soot was oxidized at 300 °C, and T_m was reduced by 178−250 °C, indicating that the prepared catalysts with different facet shapes exhibited high catalytic activity at low temperatures. Among them, the nanoflower-shaped Co-f exhibited the best low-temperature oxidation activity, followed by the nanoplate-shaped Co-p and

Table 1. Comparative Activity Evaluation of Some Co_3O_4 Catalysts Reported in the Literature for Soot Oxidation

catalysts	T_{50}/°C	T_{90}/°C	T_m/°C	Reference
without catalyst	609	638	620	this work
Co-c	438	535	442	this work
Co-p	382	513	386	this work
Co-f	369	474	370	this work
Co_3O_4 spherical flower	437	474	482	35
Co_3O_4 urchin	406	439	440	35
Co_3O_4 sheet	377	412	405	35
Co_3O_4 pyramid	361	396	385	35
Co_3O_4 nanocubes			423	27
Co_3O_4 truncated octahedrons			435	27
Co_3O_4 octahedrons			448	27
Co_3O_4	387.3	428.7		7
Co_3O_4	580	621	600	33
Co_3O_4	545			36

https://doi.org/10.1021/acsomega.2c05550
ACS Omega 2022, 7, 44116−44123

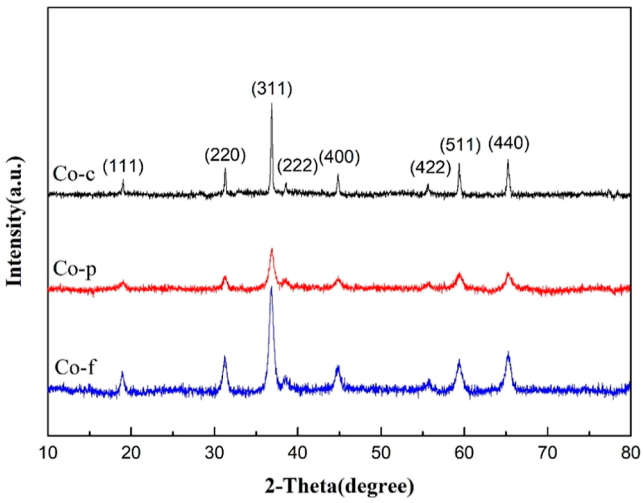

Figure 2. XRD patterns of Co_3O_4 with different nanostructures.

Table 2. Grain Diameter and Textural Properties of Co_3O_4 with Different Nanostructures

sample	peak position (°)	FWHM (°)	D (nm)	surface area ($m^2\ g^{-1}$)	average pore size (nm)	pore volume ($cm^3\ g^{-1}$)
Co-c	36.8	0.1966	42.12	5.389	10.07	0.0119
Co-p	36.8	0.6705	12.35	51.52	16.45	0.2038
Co-f	36.8	0.6662	12.43	57.09	11.50	0.1621

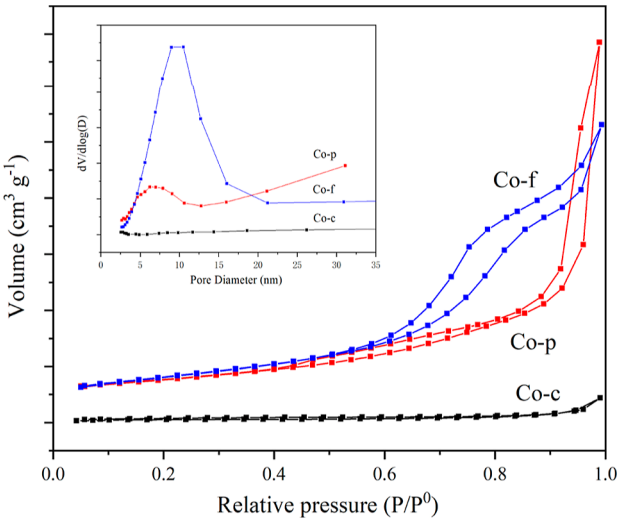

Figure 3. N_2 adsorption−desorption isotherms and pore size distributions (inset).

the nanocube-shaped Co-c. The T_m of these three catalysts was in the order Co-f < Co-p < Co-c, which is much lower than that of soot T_m = 620 °C. Co-f exhibited a high oxidation activity at low temperatures; its T_{50}, T_{90}, and T_m were only 369, 474, and 370 °C, respectively. The results show that the soot oxidation activity of Co-f was higher than that of Co-p and Co-c at low temperatures. After three cycles of experiments, the activity of Co-f oxidized soot remained stable. The activity of Co-c was the poorest.

3.2. Characterization of the Catalysts. *3.2.1. XRD Analysis.* The crystal structures of the Co_3O_4 materials were examined using XRD. Figure 2 displays the XRD patterns of Co_3O_4 with different nanostructures. The three catalysts are spinel cubic Co_3O_4 phases. The characteristic peaks of the Co_3O_4 catalysts at 2θ values of 19.0, 31.3, 36.8, 38.5, 44.8, 55.6, 59.4, and 65.2°, respectively, correspond to the crystal plane parameters of spinel Co_3O_4 (111), (220), (311), (222), (400), (422), (511), and (440) (JCPDS NO.43-1003);[24,37] no other impurities were observed, and the XRD peaks of the three catalysts were strong and narrow. The catalysts exhibited high purity, and they all exhibited a high degree of crystallization. The Scherrer equation was used to calculate the crystallite size of Co_3O_4 using the main XRD peak of (311), as shown in Table 2. The grain sizes of Co-p, Co-f, and Co-c were 12.35, 12.43, and 42.12 nm, respectively. Co-c exhibited the largest grain diameter and the lowest catalytic activity combined with the performance test results of the catalysts, while Co-f and Co-p exhibited high soot catalytic activity because of their small grain diameters. Furthermore, there was little difference between the activities of Co-f and Co-p when the grain diameter was small. The catalytic activity varied with the particle size, crystallinity, and crystal shape of the catalyst. A smaller catalyst particle size indicated better carbon soot oxidation activity.

Figure 3 shows the N_2 adsorption−desorption isotherms and the pore size distributions of the three catalysts. The curves for all the catalysts exhibited classical type-IV isotherms with a hysteresis loop, showing a characteristic mesoporous structure.[38] Table 2 lists the textural properties in terms of the average pore size, Brunauer−Emmett−Teller (BET) surface area, and pore volume. The BET surface areas of Co-c, Co-p, and Co-f were 5.389, 51.52 and 57.09 $m^2\ g^{-1}$, respectively. The pore volumes of Co-c, Co-p, and Co-f were 0.0119, 0.2038, and 0.1621 $cm^3\ g^{-1}$, respectively. Co-f had the largest specific surface area and good pore volume, which is one of the main reasons for its superior catalytic activity. However, the smallest specific surface area, average pore size, and pore volume of Co-c are one of the main reasons for its poorest catalytic activity.

3.2.2. Scanning Electron Microscopy. The micromorphologies of the Co_3O_4 catalysts with different nanostructures were studied using SEM, as shown in Figure 4. Co-c, Co-p, and Co-f exist as nanocubes, nanoplates, and nanoflowers, respectively. Figure 4a shows a smooth Co_3O_4 nanocube structure with four exposed surfaces with a mean size of ∼400 nm; Figure 4b shows a rough round Co_3O_4 nanoplate structure, ∼100 nm in diameter. The material comprises irregular nanosheets with a Co_3O_4 nanoflower shape and voids of various sizes inside the nanoflower (Figure 4c). The three catalysts have good crystallinity and an unmistakable shape, which concurred with the XRD results. Co-f exhibits the best soot oxidation activity at low temperatures owing to the unique nanoflower structure, which improves the contact efficiency with soot particles and oxygen. Figure 4d shows SEM of Co-f after the reaction with soot, and its flower-like structure remains stable before and after the reaction, which is the main reason why it maintains stable catalytic activity.

3.2.3. H_2−TPR Analysis. The reducibility of Co_3O_4 catalysts with different nanostructures was investigated using H_2−TPR, which was mainly used to study the reduction ability of the catalyst samples. Figure 5 shows the H_2−TPR profiles of the three shapes of Co_3O_4 nanocrystals. All the catalysts exhibited two reduction peaks below 406 °C, suggesting that the reduction process of Co_3O_4 included two processes: from Co^{3+} to Co^{2+} and from Co^{2+} to metal Co^0.[24] For the first reduction peak of Co^{3+} to Co^{2+}, the reduction peak temperatures of Co-f and Co-p were 299 and 290 °C, respectively, which were much

https://doi.org/10.1021/acsomega.2c05550
ACS Omega 2022, 7, 44116−44123

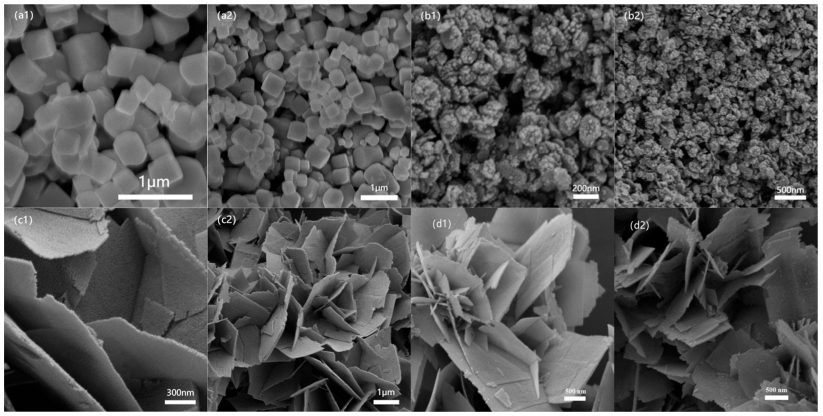

Figure 4. SEM images of different morphologies of Co_3O_4: [(a1,a2) Co-c; (b1,b2) Co-p; (c1,c2) Co-f; (d1) Co-f after the first reaction with soot; and (d2) Co-f after the third reaction with soot].

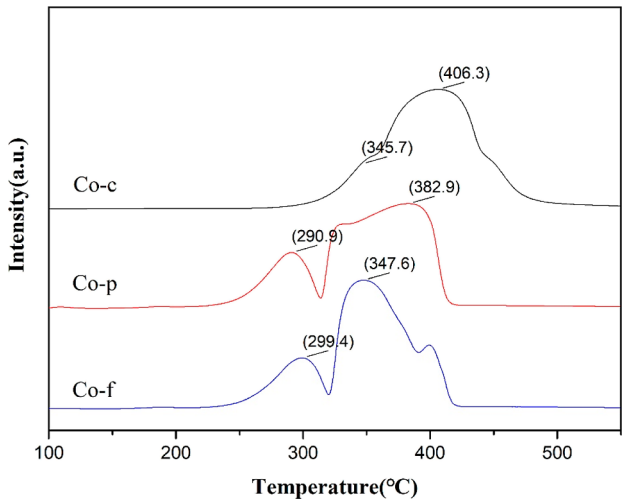

Figure 5. H_2−TPR profiles of Co_3O_4 with different nanostructures.

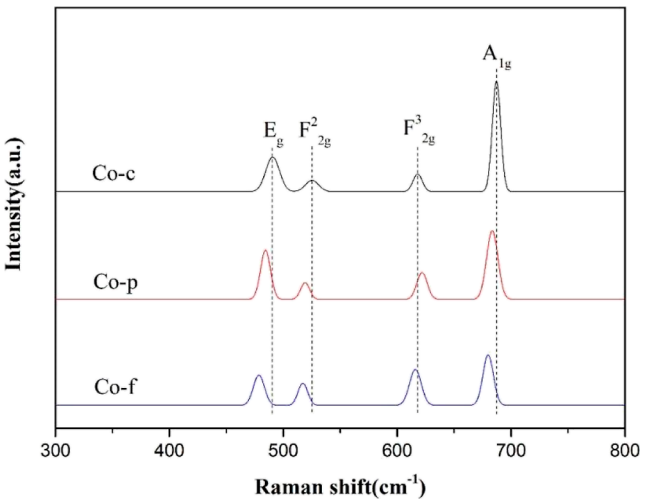

Figure 7. Raman spectra of Co_3O_4 with different nanostructures.

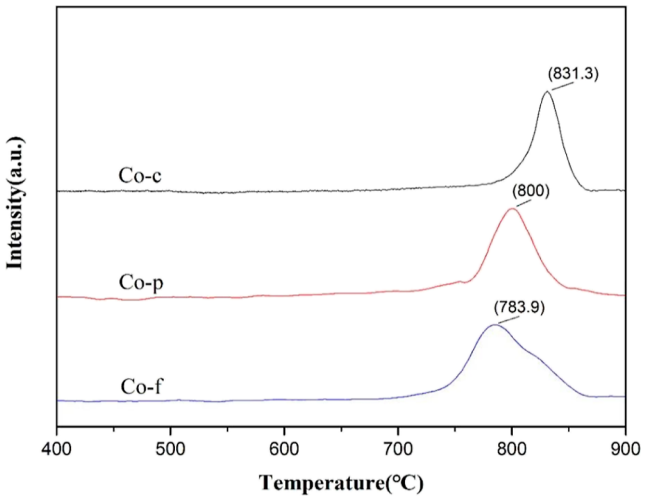

Figure 6. O_2−TPD profiles of Co_3O_4 with different nanostructures.

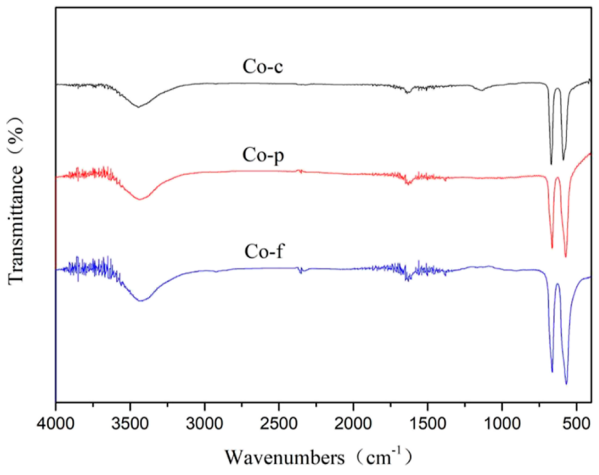

Figure 8. FTIR spectra of Co_3O_4 with different nanostructures.

lower than the reduction peak temperature of Co-c (345 °C). The second reduction peak was due to the double electron reduction process from Co^{2+} to metal Co^0. The second reduction peak of Co-f was observed at 347 °C, which was 35 and 59 °C lower than that of Co-p and Co-c, respectively. Therefore, the low-temperature reducibility of Co-f was better than that of the other two samples. Figure 5 shows that the reduction peak of Co-f shifted the most toward the low temperature. Co-f had better low-temperature reducibility than the other two samples. The Co-f reduction peak shifted toward the low-temperature portion, whereas the Co-c peak exhibited the widest temperature range. The low-temperature reducibility of the catalysts was in the order Co-f > Co-p > Co-c.

https://doi.org/10.1021/acsomega.2c05550
ACS Omega 2022, 7, 44116−44123

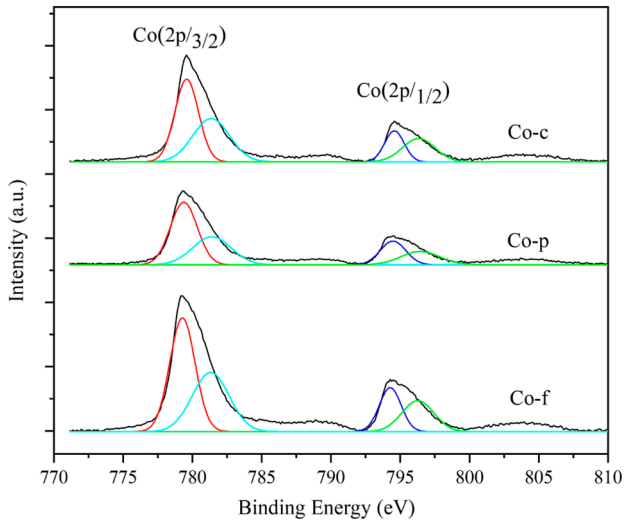

Figure 9. XPS spectra of Co 2p over Co_3O_4 with different nanostructures.

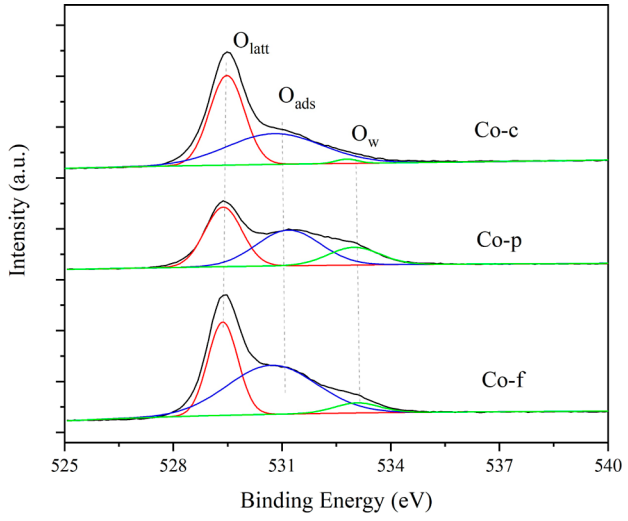

Figure 10. XPS spectra of O 1s over Co_3O_4 with different nanostructures.

This suggests that Co-f has stronger reducibility related to the catalytic activity, so the catalytic activity of Co-f for soot oxidation is the highest; this is consistent with the test results of catalyst performance.

3.2.4. O_2–TPD Analysis. Figure 6 shows the O_2–TPD diagram of the catalysts, which shows how well the catalysts can adsorb and activate oxygen. Generally, the order of oxygen desorption in metal oxides is as follows: oxygen (O_2) > oxygen molecular anion (O_2^-) > oxygen ion (O^-) > lattice oxygen (O^{2-}).[39] O_2^- and O^- are due to the molecular adsorption oxygen and chemisorption, respectively. Surface-active oxygen desorbs easily from metal oxide catalysts, whereas lattice oxygen is more challenging.[39] Figure 6 shows a desorption peak at ∼800 °C owing to the large amount of lattice oxygen precipitated during the thermal decomposition of Co_3O_4. The lowest desorption peak temperature of Co-f was 783 °C, followed by Co-p (800 °C). The highest desorption peak temperature of Co-c was 831 °C. Co-f can decompose a large amount of lattice oxygen at lower temperatures, showing better activation performance. Co-f had the largest desorption peak area and the highest concentration of surface-decomposed lattice oxygen, exhibiting the best catalytic capacity for soot oxidation; the results are consistent with those of H_2–TPR.

3.2.5. Raman Analysis. Figure 7 shows the Raman spectra of all the catalysts. Four obvious peaks were observed at 486 cm^{-1} (E_g), 524 cm^{-1} (F_{2g}^2), 622 cm^{-1} (F_{2g}^3), and 692 cm^{-1} (A_{1g}), which are consistent with the characteristics of the spinel Co_3O_4 phase.[27] No other impurity peaks are found, which is consistent with the results of XRD. The XRD peak of the catalyst shifts to a low wavenumber, and the FWHM increases in the order Co-f > Co-p > Co-c, which may be related to the high-defect structure of the spinel. The increase in the surface defect structure of the catalyst was beneficial to the formation of oxygen vacancies, which promoted the adsorption and activation of oxygen species and subsequently promoted soot oxidation. Among them, the defect structure of Co-f was more than that of Co-p and Co-c, so it exhibited higher soot oxidation activity. This is consistent with the abovementioned results of H_2–TPR and O_2–TPD.

3.2.6. Fourier Transform Infrared Spectroscopy. The FTIR spectra of the catalysts showed four absorption peaks in the 400–4000 cm^{-1} range (Figure 8), in which the absorption peak at 3450 cm^{-1} corresponds to the characteristic peak of the stretching vibration of the OH group in $Co(OH)_2$. The absorption peak at 1630 cm^{-1} was caused by the stretching vibration of NO_3^-, and the absorption peaks at 667 and 590 cm^{-1} were caused by the stretching vibration of Co–O in the metal oxide lattice.[40] A characteristic peak of NO_3^- was observed in the spectrum, but NO_3^- was not detected by XRD because NO_3^- entered the structure and did not form a chemical bond with $Co(OH)_2$, which explains why there was no hydrogen bonding in the structure. No characteristic peak of stretching vibration of Co–OH was observed in the spectra (Figure 8), indicating that all the final products had transformed to a pure phase Co_3O_4. The change in the abovementioned stretching vibration absorption peak reflected the change in the phase structure of the catalysts during the synthesis process, which was consistent with the XRD results.

3.2.7. X-ray Photoelectron Spectroscopy Analysis. The surface element composition and valence state of Co_3O_4 nanocrystals were measured using XPS, including Co 2p and O 1s photoelectron spectroscopy. Figure 9 shows the Co 2p spectra of the catalysts. The Co 2p spectra of Co_3O_4 nanocrystals have two main peaks near 780 and 795 eV, which were assigned to Co $2p_{3/2}$ and Co $2p_{1/2}$ orbitals, respectively. The difference in BE between Co $2p_{3/2}$ and Co

Table 3. BE of the Co 2p and O 1s Core Levels and the Ratio of Co^{3+}/Co^{2+} and O_{ads}/O_{latt} for the As-Prepared Catalysts

	Co 2p			O 1s		
catalysts	Co^{2+} (eV)	Co^{3+} (eV)	$Co^{3+}/(Co^{2+} + Co^{3+})$	O_{ads} (eV)	O_{latt} (eV)	$O_{ads}/(O_{ads} + O_{latt})$
Co-c	781.3/796.5	779.6/794.6	0.527	530.9	529.5	0.479
Co-p	781.4/796.6	779.3/794.4	0.551	531.1	529.4	0.506
Co-f	781.4/796.3	779.2/794.3	0.592	530.8	529.4	0.603

https://doi.org/10.1021/acsomega.2c05550
ACS Omega 2022, 7, 44116–44123

$2p_{1/2}$ peaks was 15 eV, showing that cobalt oxides existed in the form of Co_3O_4, which is in accordance with a previous report.[24] Both Co $2p_{3/2}$ (~779.3 eV) and Co $2p_{1/2}$ (~794.7 eV) were attributed to the characteristic peaks of Co^{3+} cations, while the characteristic peaks in Co $2p_{3/2}$ (near 781.6 eV) and Co $2p_{1/2}$ (near 796.5 eV) generally belonged to Co^{2+} in the catalysts.[27] The characteristic peak intensity of Co^{2+} cations was small, indicating only a small part of Co^{2+} in Co_3O_4 nanocrystals, mainly in the form of Co^{3+}. The ratio of $Co^{3+}/(Co^{2+} + Co^{3+})$ of Co-f was considerably higher than that of Co-c and Co-p, indicating more exposed Co^{3+} on the surface of Co-f because of its unique nanoflower structure and small particle size. More Co^{3+} on the catalyst surface affords higher catalytic activity.

Figure 10 shows the O 1s XPS spectra of the Co_3O_4 nanocrystals. The spectra of O 1s can be deconvoluted into three peaks with their BE near 529.4, 530.9, and 533.1 eV, belonging to the surface lattice oxygen (O_{latt}: O^{2-}), surface chemisorbed oxygen (O_{ads}: O_2^{2-} and O_2^-), and chemisorbed water (O_w), respectively.[41] Typically, the $O_{ads}/(O_{ads} + O_{latt})$ ratio represents the active oxygen content on the catalyst surface. The active oxygen content and catalytic activity increase with increasing molar ratio.[42] The $O_{ads}/(O_{ads} + O_{latt})$ ratio decreased in the following order (Figure 10 and Table 3): Co-f > Co-p > Co-c, which was consistent with the sequence of catalytic activity. Co-f, possessing more Co^{3+} and O_{ads} species, exhibited better catalytic performance.

4. CONCLUSIONS

A series of Co_3O_4 materials with various nanostructures, including nanocubes, nanoplates, and nanoflowers, were synthesized using a simple template-free hydrothermal method and showed excellent catalytic activity for the oxidation of soot particles. The three types of nanostructured Co_3O_4 crystals produced had exceptional purity and crystallinity, which exhibited clear cubic, plate-like, and floral morphologies. The Co_3O_4 nanoflowers showed better soot oxidation activity than the Co_3O_4 nanocubes and nanoplates because of the presence of a large number of Co^{3+} cations and a large amount of lattice oxygen on the surface of Co_3O_4 nanoflowers prone to low-temperature redox reactions. The Co_3O_4 nanoflowers have highly defective structures, which are favorable for the formation of oxygen vacancies, promoting the adsorption and activation of oxygen species for soot oxidation. Furthermore, Co_3O_4 nanoflowers have a good shape and spatial structure, increasing the contact area with soot particles and yielding improved soot catalytic efficiency. However, Co_3O_4 nanocubes had the poorest catalytic performance. This is mostly because of their large grain size and less defective surface structure, affording poor redox ability and less lattice oxygen. One of the key factors to achieve improved catalytic activity is increasing the contact area between the catalysts and soot particles.

AUTHOR INFORMATION

Corresponding Authors

Chao Hu − *Anhui Advanced Technology Research Institute of Green Building, Department of Building Environment and Thermal Engineering, School of Environment and Energy Engineering, Anhui Jianzhu University, Hefei 230601, China*; orcid.org/0000-0002-6036-0548; Phone: +86 55163828252; Email: chaohu@mail.ustc.edu.cn

Haitao Zhang − *Anhui Special Equipment Inspection Institute, Hefei 230601, China*; Email: jayzht@mail.ustc.edu.cn

Authors

PengCheng Dai − *Anhui Advanced Technology Research Institute of Green Building, Department of Building Environment and Thermal Engineering, School of Environment and Energy Engineering, Anhui Jianzhu University, Hefei 230601, China*

Zhenzhen Chen − *Anhui Advanced Technology Research Institute of Green Building, Department of Building Environment and Thermal Engineering, School of Environment and Energy Engineering, Anhui Jianzhu University, Hefei 230601, China*

Complete contact information is available at: https://pubs.acs.org/10.1021/acsomega.2c05550

Notes

The authors declare no competing financial interest.

ACKNOWLEDGMENTS

This work was supported by the Natural Science Foundation of Anhui Province (2008085QE263), the Anhui Provincial Key Research and Development Project (no.2022107020013), and the Science and Technology Plan Project of Anhui Market Supervision Administration (no.2019MK030). We also thank Wang from Shiyanjia Lab (www.shiyanjia.com) for the XPS analysis. The authors gratefully acknowledge all the support.

REFERENCES

(1) Wu, Q.; Jing, M.; Wei, Y.; Zhao, Z.; Zhang, X.; Xiong, J.; Liu, J.; Song, W.; Li, J. High-efficient catalysts of core-shell structured Pt@transition metal oxides (TMOs) supported on 3DOM-Al_2O_3 for soot oxidation: The effect of strong Pt-TMO interaction. *Appl. Catal., B* **2019**, *244*, 628−640.

(2) Lin, Y.; Zhu, B.; Chen, J.; Wu, J.; Lu, K.; Gu, M.; Chu, H. Study of soot functional groups and morphological characteristics in laminar coflow methane and ethylene diffusion flames with hydrogen addition. *Fuel* **2020**, *279*, 118474.

(3) Browne, E. C.; Franklin, J. P.; Canagaratna, M. R.; Massoli, P.; Kirchstetter, T. W.; Worsnop, D. R.; Wilson, K. R.; Kroll, J. H. Changes to the chemical composition of soot from heterogeneous oxidation reactions. *J. Phys. Chem. A* **2015**, *119*, 1154−1163.

(4) Ruiz, M. P.; Callejas, A.; Millera, A.; Alzueta, M. U.; Bilbao, R. Soot formation from C_2H_2 and C_2H_4 pyrolysis at different temperatures. *J. Anal. Appl. Pyrolysis* **2007**, *79*, 244−251.

(5) Prasad, R.; Singh, S. V. A review on catalytic oxidation of soot emitted from diesel fuelled engines. *J. Environ. Chem. Eng.* **2020**, *8*, 103945.

(6) Shang, Z.; Sun, M.; Chang, S.; Che, X.; Cao, X.; Wang, L.; Guo, Y.; Zhan, W.; Guo, Y.; Lu, G. Activity and stability of Co_3O_4-based catalysts for soot oxidation: The enhanced effect of Bi_2O_3 on activation and transfer of oxygen. *Appl. Catal., B* **2017**, *209*, 33−44.

(7) Chen, L.; Li, T.; Zhang, J.; Wang, J.; Chen, P.; Fu, M.; Wu, J.; Ye, D. Chemisorbed superoxide species enhanced the high catalytic performance of Ag/Co_3O_4 nanocubes for soot oxidation. *ACS Appl. Mater. Interfaces* **2021**, *13*, 21436−21449.

(8) Zhai, G.; Wang, J.; Chen, Z.; Yang, S.; Men, Y. Highly enhanced soot oxidation activity over 3DOM Co_3O_4-CeO_2 catalysts by synergistic promoting effect. *J. Hazard. Mater.* **2019**, *363*, 214−226.

(9) Liu, H.; Dai, X.; Wang, K.; Yan, Z.; Qian, L. Highly efficient catalysts of $Mn_{1-x}Ag_xCo_2O_4$ spinel oxide for soot combustion. *Catal. Commun.* **2017**, *101*, 134−137.

(10) Xiong, J.; Wu, Q.; Mei, X.; Liu, J.; Wei, Y.; Zhao, Z.; Wu, D.; Li, J. Fabrication of Spinel-Type $Pd_xCo_{3-x}O_4$ Binary Active Sites on 3D Ordered Meso-macroporous Ce-Zr-O_2 with Enhanced Activity for Catalytic Soot Oxidation. *ACS Catal.* **2018**, *8*, 7915−7930.

(11) Gao, Y.; Yu, Q.; Du, Y.; Yang, M.; Gao, L.; Rao, S.; Yang, Z.; Lan, Q.; Yang, Z. Synthesis of Co_3O_4-NiO nano-needles for

https://doi.org/10.1021/acsomega.2c05550
ACS Omega 2022, 7, 44116−44123

amperometric sensing of glucose. *J. Electroanal. Chem.* **2019**, *838*, 41−47.
(12) Zhao, H.; Li, H.; Pan, Z.; Feng, F.; Gu, Y.; Du, J.; Zhao, Y. Design of CeMnCu ternary mixed oxides as soot combustion catalysts based on optimized Ce/Mn and Mn/Cu ratios in binary mixed oxides. *Appl. Catal., B* **2020**, *268*, 118422.
(13) Medina, J. C.; Rodil, S. E.; Zanella, R. Synthesis of a CeO_2/Co_3O_4 catalyst with a remarkable performance for the soot oxidation reaction. *Catal. Sci. Technol.* **2020**, *10*, 853−863.
(14) Ghiassee, M.; Rezaei, M.; Meshkani, F.; Mobini, S. Preparation of the Mn/Co mixed oxide catalysts for low-temperature CO oxidation reaction. *Environ. Sci. Pollut. Res.* **2021**, *28*, 379−388.
(15) Wei, Y.; Liu, J.; Zhao, Z.; Duan, A.; Jiang, G. The catalysts of three-dimensionally ordered macroporous $Ce_{1-x}Zr_xO_2$ supported gold nanoparticles for soot combustion: The metal−support interaction. *J. Catal.* **2012**, *287*, 13−29.
(16) Nguyen, H.; El-Safty, S. A. Meso- and Macroporous Co_3O_4 nanorods for effective VOC gas sensors. *J. Phys. Chem. C* **2011**, *115*, 8466−8474.
(17) Xia, S.; Yu, M.; Hu, J.; Feng, J.; Chen, J.; Shi, M.; Weng, X. A model of interface-related enhancement based on the contrast between Co_3O_4 sphere and cube for electrochemical detection of hydrogen peroxide. *Electrochem. Commun.* **2014**, *40*, 67−70.
(18) Xu, G.; Li, J.; Huang, L.; Lin, W.; Sun, S. Synthesis of Co_3O_4 nano-octahedra enclosed by {111} facets and their excellent lithium storage properties as anode material of lithium ion batteries. *Nano Energy* **2013**, *2*, 394−402.
(19) Xiao, X.; Liu, X.; Zhao, H.; Chen, D.; Liu, F.; Xiang, J.; Hu, Z.; Li, Y. Facile Shape Control of Co_3O_4 and the Effect of the Crystal Plane on Electrochemical Performance. *Adv. Mater.* **2012**, *24*, 5762−5766.
(20) Wang, X.; Yu, L.; Wu, X. L.; Yuan, F.; Guo, Y. G.; Ma, Y.; Yao, J. Synthesis of single-crystalline Co_3O_4 octahedral cages with tunable surface aperture and their lithium storage properties. *J. Phys. Chem. C* **2009**, *113*, 15553−15558.
(21) Ouyang, B.; Xiong, S.; Zhang, Y.; Liu, B.; Li, J. The study of morphology effect of Pt/Co_3O_4 catalysts for higher alcohol synthesis from CO_2 hydrogenation. *Appl. Catal., A* **2017**, *543*, 189−195.
(22) Wang, Y.; Zhou, L.; Duan, X.; Sun, H.; Tin, E. L.; Jin, W.; Wang, S. Photochemical degradation of phenol solutions on Co_3O_4 nanorods with sulfate radicals. *Catal. Today* **2015**, *258*, 576−584.
(23) Hu, L.; Peng, Q.; Li, Y. Selective synthesis of Co_3O_4 nanocrystal with different shape and crystal plane effect on catalytic property for methane combustion. *J. Am. Chem. Soc.* **2008**, *130*, 16136−16137.
(24) Ren, Q.; Feng, Z.; Mo, S.; Huang, C.; Li, S.; Zhang, W.; Chen, L.; Fu, M.; Wu, J.; Ye, D. 1D-Co_3O_4, 2D-Co_3O_4, 3D-Co_3O_4 for catalytic oxidation of toluene. *Catal. Today* **2019**, *332*, 160−167.
(25) Wang, K.; Cao, Y.; Hu, J.; Li, Y.; Xie, J.; Jia, D. Solvent-Free Chemical Approach to Synthesize Various Morphological Co_3O_4 for CO Oxidation. *ACS Appl. Mater. Interfaces* **2017**, *9*, 16128−16137.
(26) Hu, L.; Sun, K.; Peng, Q.; Xu, B.; Li, Y. Surface active sites on Co_3O_4 nanobelt and nanocube model catalysts for CO oxidation. *Nano Res.* **2010**, *3*, 363−368.
(27) Zhai, G.; Wang, J.; Chen, Z.; An, W.; Men, Y. Boosting soot combustion efficiency of Co_3O_4 nanocrystals via tailoring crystal facets. *Chem. Eng. J.* **2018**, *337*, 488−498.
(28) Deng, X.; Li, M.; Zhang, J.; Hu, X.; Zheng, J.; Zhang, N.; Chen, B. H. Constructing nano-structure on silver/ceria-zirconia towards highly active and stable catalyst for soot oxidation. *Chem. Eng. J.* **2017**, *313*, 544−555.
(29) Jian, S.; Yang, Y.; Ren, W.; Xing, L.; Zhao, D.; Tian, Y.; Ding, T.; Li, X. Kinetic analysis of morphologies and crystal planes of nanostructured CeO_2 catalysts on soot oxidation. *Chem. Eng. Sci.* **2020**, *226*, 115891.
(30) Hu, C.; Chen, Z.; Wei, C.; Wan, X.; Li, W.; Lin, Q. Au Nanoparticles Supported on Iron-Based Oxides for Soot Oxidation: Physicochemical Properties Before and After the Reaction. *ACS Omega* **2021**, *6*, 11510−11518.
(31) Corro, G.; Cebada, S.; Pal, U.; Fierro, J. L. G. Au^0−Au^{3+} bifunctional site mediated enhanced catalytic activity of Au/ZnO composite in diesel particulate matter oxidation. *J. Catal.* **2017**, *347*, 148−156.
(32) Guan, B.; Huang, Y.; Lin, H.; Huang, Z. Promoting Effects of Barium Substitution on the Catalytic Performances of $FeCeO_{2-\delta}$ for Soot Oxidation. *Ind. Eng. Chem. Res.* **2018**, *57*, 8635−8646.
(33) Zhang, S.; Zhu, X.; Zheng, C.; Hu, D.; Zhang, J.; Gao, X. Study on catalytic soot oxidation over spinel type ACo_2O_4 (A = Co, Ni, Cu, Zn) catalysts. *Aerosol Air Qual. Res.* **2017**, *17*, 2317−2327.
(34) Xing, L.; Yang, Y.; Ren, W.; Zhao, D.; Tian, Y.; Ding, T.; Zhang, J.; Zheng, L.; Li, X. Highly efficient catalytic soot combustion performance of hierarchically meso-macroporous Co_3O_4/CeO_2 nanosheet monolithic catalysts. *Catal. Today* **2020**, *351*, 83−93.
(35) Tsai, Y. C.; Nhat Huy, N. N.; Lee, J.; Lin, Y. F.; Lin, K. Y. A. Catalytic soot oxidation using hierarchical cobalt oxide microspheres with various nanostructures: Insights into relationships of morphology, property and reactivity. *Chem. Eng. J.* **2020**, *395*, 124939.
(36) Shang, Z.; Sun, M.; Che, X.; Wang, W.; Wang, L.; Cao, X.; Zhan, W.; Guo, Y.; Guo, Y.; Lu, G. The existing states of potassium species in K-doped Co_3O_4 catalysts and their influence on the activities for NO and soot oxidation. *Catal. Sci. Technol.* **2017**, *7*, 4710−4719.
(37) Cao, C.; Xing, L.; Yang, Y.; Tian, Y.; Ding, T.; Zhang, J.; Hu, T.; Zheng, L.; Li, X. Diesel soot elimination over potassium-promoted Co_3O_4 nanowires monolithic catalysts under gravitation contact mode. *Appl. Catal., B* **2017**, *218*, 32−45.
(38) Yang, W.; Li, X.; Jiang, Z.; Li, C.; Zhao, J.; Wang, H.; Liao, Q. Structure-dependent catalysis of Co_3O_4 crystals in persulfate activation via nonradical pathway. *Appl. Surf. Sci.* **2020**, *525*, 146482.
(39) Lei, Y.; Li, W.; Liu, Q.; Lin, Q.; Zheng, X.; Huang, Q.; Guan, S.; Wang, X.; Wang, C.; Li, F. Typical crystal face effects of different morphology ceria on the activity of Pd/CeO_2 catalysts for lean methane combustion. *Fuel* **2018**, *233*, 10−20.
(40) Zhou, T.; Lu, P.; Zhang, Z.; Wang, Q.; Umar, A. Perforated Co_3O_4 nanoneedles assembled in chrysanthemum-like Co_3O_4 structures for ultra-high sensitive hydrazine chemical sensor. *Sens. Actuators, B* **2016**, *235*, 457−465.
(41) Wei, Y.; Zhang, Y.; Zhang, P.; Xiong, J.; Mei, X.; Yu, Q.; Zhao, Z.; Liu, J. Boosting the removal of diesel soot particles by the optimal exposed crystal facet of CeO_2 in Au/CeO_2 catalysts. *Environ. Sci. Technol.* **2019**, *54*, 2002−2011.
(42) Ji, F.; Men, Y.; Wang, J.; Sun, Y.; Wang, Z.; Zhao, B.; Tao, X.; Xu, G. Promoting diesel soot combustion efficiency by tailoring the shapes and crystal facets of nanoscale Mn_3O_4. *Appl. Catal., B* **2019**, *242*, 227−237.

https://doi.org/10.1021/acsomega.2c05550
ACS Omega 2022, 7, 44116−44123